



Identification of Frataxin as a regulator of ferroptosis

Jing Du^{a,1}, Yi Zhou^{c,f,1}, Yanchun Li^{c,1}, Jun Xia^a, Yongjian Chen^a, Sufeng Chen^a, Xin Wang^d, Weidong Sun^{e,h}, Tongtong Wang^f, Xueying Ren^a, Xu Wang^g, Yihan An^h, Kang Lu^h, Wanye Hu^h, Siyuan Huang^c, Jianghui Li^g, Xiangmin Tong^{a,b,c,d,g,h,**}, Ying Wang^{b,d,h,*}

^a Department of Laboratory Medicine, Zhejiang Provincial People's Hospital, People's Hospital of Hangzhou Medical College, Hangzhou, Zhejiang, 310014, China

^b Phase I Clinical Research Center, Zhejiang Provincial People's Hospital, People's Hospital of Hangzhou Medical College, Hangzhou, Zhejiang, 310014, China

^c The Second Clinical Medical School of Zhejiang Chinese Medical University, Zhejiang Chinese Medical University, Hangzhou, Zhejiang, 310053, China

^d Clinical Research Institute, Zhejiang Provincial People's Hospital, People's Hospital of Hangzhou Medical College, Hangzhou, Zhejiang, 310014, China

^e Department of Hematology, Shaoxing Central Hospital, Shaoxing, Zhejiang, 312030, China

^f Department of Wangjiangshan, Zhejiang Provincial People's Hospital, People's Hospital of Hangzhou Medical College, Hangzhou, Zhejiang, 310014, China

^g School of Laboratory Medicine and Life Science, Wenzhou Medical University, Wenzhou, Zhejiang, 325035, China

^h Bengbu Medical College, Bengbu, Anhui, 233000, China

ARTICLE INFO

Keywords:

Ferroptosis
Frataxin
Iron-sulfur cluster
Mitochondria

ABSTRACT

Ferroptosis is a newly discovered form of non-apoptotic regulated cell death and is characterized by iron-dependent and lipid peroxidation. Due to the enhanced dependence on iron in cancer cells, induction of ferroptosis is becoming a promising therapeutic strategy. However, the precise underlying molecular mechanism and regulation process of ferroptosis remains largely unknown. In the present study, we demonstrate that the protein Frataxin (FXN) is a key regulator of ferroptosis by modulating iron homeostasis and mitochondrial function. Suppression of FXN expression specifically repressed the proliferation, destroyed mitochondrial morphology, impeded Fe-S cluster assembly and activated iron starvation stress. Moreover, suppression of FXN expression significantly enhanced erastin-induced cell death through accelerating free iron accumulation, lipid peroxidation and resulted in dramatic mitochondria morphological damage including enhanced fragmentation and vanished cristae. In addition, this type of cell death was confirmed to be ferroptosis, since it could be pharmacologically restored by ferroptotic inhibitor Fer-1 or GSH, but not by inhibitors of apoptosis, necrosis. Vice versa, enforced expression of FXN blocked iron starvation response and erastin-induced ferroptosis. More importantly, pharmacological or genetic blocking the signal of iron starvation could completely restore the resistance to ferroptosis in FXN knockdown cells and xenograft *in vivo*. This paper suggests that FXN is a novel ferroptosis modulator, as well as a potential provided target to improve the antitumor activity based on ferroptosis.

1. Introduction

Despite success in chemotherapy drugs clinically, drug toxicity and resistance continue to be the principal limiting factor to achieving cures in patients with cancer. Activation of regulated cell death and exploration therapy targets with less toxicity is a potential anticancer treatment strategy. Numerous therapy targets have been discovered for that cancer is a heterogeneous disease defined by various genetic and epigenetic variations. But little is known about the molecular biological characteristics of mitochondrial protein Frataxin (FXN) in cancer.

Iron is an indispensable element for various metabolic and physiological functions in living organisms. It functions as a cofactor for vital iron-containing enzymes that are involved in DNA synthesis, ATP production, heme synthesis and many other physiological activities [1]. In general, a certain amount of iron is crucial for cell survival, growth and proliferation. Therefore, iron deficiency is undoubtedly deleterious, leading to a multisystem disorder with innumerable effects, including anemia [2]. Conversely, too much iron is also detrimental. The aberrant accumulation of iron causes excess free radical generation through Fenton reaction and subsequent results in significant alterations in the

* Corresponding author. Phase I Clinical Research Center, Zhejiang Provincial People's Hospital, People's Hospital of Hangzhou Medical College, Hangzhou, Zhejiang, 310014, China.

** Corresponding author. Phase I Clinical Research Center, Zhejiang Provincial People's Hospital, People's Hospital of Hangzhou Medical College, Hangzhou, Zhejiang, 310014, China.

E-mail addresses: tongxiangming@hmc.edu.cn (X. Tong), wangying@hmc.edu.cn (Y. Wang).

¹ These authors contributed equally to this work.

cellular redox homeostasis, thus leading to the damage of DNA, proteins or other biomolecules. Interestingly, relative to healthy cells, cancer cells do exhibit an enhanced dependence on iron to enable its growth, which may act as a target for cancer therapy [3]. It is noted that iron overload can cause a specific cell death termed as ferroptosis, which is a recently discovered form of non-apoptotic regulated necrosis [4]. Ferroptosis has been implicated in the pathological process associated with carcinogenesis, degenerative diseases, stroke, and kidney ischemia/reperfusion (I/R) injury [5–8]. However, the precise underlying molecular mechanism and potential anticancer therapeutic significance of ferroptosis remain to be elucidated.

The execution of ferroptosis closely involves the iron-dependent peroxidation of polyunsaturated fatty acids (PUFAs) [9]. Since mitochondria employ the majority of cellular iron, it plays a critical role in the iron homeostasis. The excess iron leads to a disturbance in mitochondrial dynamics and even results in ferroptosis. The cystine/glutamate antiporter inhibitor erastin and GPX4 inhibitor RSL3 accelerate the progression of ferroptosis, which inhibited by the iron chelator, GSH, ferrostatin-1 and its analogs. In addition, degradation of ferritin by ferritinophagy can release free iron and initiate the process of ferroptosis [10,11]. Cancer cells harboring oncogenic Ras exhibit sensitivity to ferroptosis and can be selectively killed. Our previous study has provided experimental evidence that dihydroartemisinin, the semi-synthetic derivatives, represents a promising therapeutic effect to preferentially target AML cells by inducing ferroptotic cell death [12]. Daolin Tang and co-workers also discovered the ferroptosis inducer erastin enhanced the sensitivity of AML cells to chemotherapeutic agents [13]. Here we focus on exploring targets to improve the sensitivity for ferroptosis in cancer cells.

The ancient and conservative cofactors, iron-sulfur cluster (ISC), are essential for biological processes such as redox reactions, iron homeostasis, enzymatic catalysis, heme synthesis and regulation of gene expression [14]. More than 60 human proteins bind with different types of ISCs to execute their functions. ISC assembly genes encode in the nuclear genome and translocate into mitochondria for creating cofactors. In humans, the de novo of Fe–S cluster biogenesis is initiated with the removal of sulfur from cysteine by the cysteine desulfurase complex Nfs1-Isd11, a process activated by frataxin [15]. The removed persulfide intermediately reduces to sulfide with the accomplished of ferredoxin reductase and ferredoxin 2, and delivers to scaffold protein ISCU to form a [2Fe–2S] cluster with ferrous iron (Fe^{2+}). Neosynthesized ISCs are then transferred to mitochondrial recipients or further assembled into [4Fe–4S] with the help of the HSC20/HSPA9 chaperone system [16]. The exact molecular function of FXN is unclear, but it has been proposed to be an iron chaperone or an allosteric activator of cysteine binding to NFS1 [15]. Defects in the biogenesis of Fe/S protein are associated with human disorders, which called Fe–S diseases. An expansion of the GAA repeat in the first intron of the FXN gene would result in the diminished expression of the encoded protein, thus leading to Friedreich's ataxia (FRDA), a most common recessive ataxia in the Caucasian population. Complete depletion of FXN is embryonically lethal in mice demonstrating its extremely vital biological function [17]. Decreased expression of FXN in FRDA is characterized as mitochondrial iron accumulation, mitochondrial dysfunction and increased oxidative stress [18]. The newly published paper demonstrated that ferroptosis inhibitors might have therapeutic potential in primary FRDA patient-derived fibroblasts [19]. Despite the central role of FXN in Fe–S assembly and FRDA, it remains unclear whether it plays a pivotal role in cancer biologic behavior and prognosis.

Indeed, our study demonstrated suppression of FXN expression specifically destroyed mitochondrial morphology, impeded Fe–S cluster assembly and enhanced cysteine deprivation-induced cell death in HT-1080 cells. This type of cell death could be pharmacologically restored by ferroptotic inhibitor Fer-1 or GSH, but not by inhibitors of apoptosis, necrosis. Moreover, the observed phenotypes of increased lipid ROS, accumulation of free iron and mitochondria dysfunction could be

rescued by ectopic expression of FXN. Additionally, pharmacological or genetic blocking the signal of iron starvation could completely restore the resistance to ferroptosis in FXN knockdown cells. This study is the first to discover the role of FXN in molecular biological characteristics of cancer and to identify the link between FXN and ferroptosis. Meanwhile, our work sheds new light on the molecular mechanisms underlying FXN induced ferroptosis through mitochondrial dysfunction as well as activation of iron starvation response, and discoveries that the ISC assembly is tightly correlated with the cancer progression, which can be developed as a potential therapeutic strategy.

2. Materials and methods

2.1. Antibodies and reagents

The antibody to Frataxin (ab219414), to Aconitase 2 (ab129069), to Aconitase 1 (ab126595), to IREB2 (ab181153), to NDUFV2 (ab183717), to FECH (ab137042), to Transferrin Receptor (ab80194), SDHB (ab14714), to Ferritin Heavy Chain (ab65080), to beta Actin (ab8226) and N-acetylcysteine (NAC), glutathione (GSH) and DCFH-DA were obtained from Abcam (Cambridge, MA). CCK-8 Assay Kit was obtained from Meilunbio (Dalian, China). CFDA-SE, GSH Assay Kit was purchased from Beyotime (Shanghai, China). Erastin, Sorafenib, Ferrostatin-1, Z-VAD-FMK, Necrostatin were obtained from Selleck Chemicals (Houston, TX). C11-BODIPY (581/591), TMRE, MitoTracker were obtained from Thermo Fisher Scientific (Waltham, MA). The Cell Cycle Staining Kit was purchased from MultiSciences (Hangzhou, China).

2.2. Cell culture

Human fibrosarcoma HT-1080 cells were obtained from the Cell Bank of Chinese Academy of Sciences (Shanghai, China) and cultured in DMEM medium (Hyclone, Logan, UT, USA) containing 10% fetal bovine serum (Gibco, Grand Island, NY, USA), supplementary with 100 U/mL penicillin and 100 $\mu\text{g}/\text{mL}$ streptomycin. Cells were maintained in an incubator with a humidified atmosphere of 5% CO_2 at 37 °C.

2.3. Cell viability assay

Cell viability assay was evaluated using the CCK8 Assay Kit. HT-1080 cells were seeded at a density of 4×10^4 cells/well in 100 μl DMEM medium in the 96-well plate for overnight, followed by treatment with different doses of erastin for 12 h. 10 μl CCK-8 was added to each well and the cells were subsequently incubated at 37 °C for 2 h. Absorbance was measured at 450 nm using the microplate reader.

2.4. PI staining

Cells were plated in 96-well plates at a density of 4×10^4 cells/well and treated with the indicated concentration of erastin. Propidium iodide (PI) was then added to each well at a final concentration of 10 $\mu\text{g}/\text{mL}$ for 10 min in the dark, and cells were subjected to fluorescence microscopy.

2.5. Transwell assay

HT-1080 cells (4×10^4) in 200 μl serum-free DMEM medium were seeded onto the upper transwell chambers, while 500 μl medium containing 5% FBS was added to the lower chambers. The cells were cultured at 37 °C in an incubator for 24 h. The transwell chambers were then removed, washed with PBS twice, fixed in 4% paraformaldehyde for 30 min and stained with 0.1% crystal violet for 20 min at room temperature. Next, PBS was used to wash chambers, and the un-migrated cells in the upper transwell membrane were gently wiped off using a cotton swab. Images were observed and photographed using an

inverted light microscope.

2.6. Cell growth assay

HT-1080 cells were seeded in a 96-well plate at a density of 3×10^3 cells/well in 100 μ l DMEM medium containing 10% FBS. The cells were incubated overnight at 37 °C in an incubator. From the second day after plating, the numbers of cells were measured at the specified time using the CCK8 Assay Kit. Next, a microplate reader was used to measure the absorbance at 450 nm.

2.7. Cell proliferation assay

Cell proliferation was detected using a CFDA-SE probe. Briefly, HT-1080 cells stained with CFDA-SE according to the manufacturer's protocol and seeded in 6-well plates. Then, cells were exposed to the same concentration of erastin. CFDA-SE fluorescence was detected by the flow cytometry.

2.8. Cell cycle analysis

Cell cycle profiles were examined by the Cell cycle staining Kit (MultiSciences, Hangzhou, China) according to the manufacturer's instructions. Briefly, cells were harvested, washed and fixed in ice-cold 70% ethanol at 4 °C overnight. Then they were washed, treated with 100 μ l RNase A at 37 °C for 30 min and stained with 400 μ l PI at 4 °C in the dark for 30 min. Finally, the cells were washed and analyzed by flow cytometry.

2.9. Colony formation assay

3×10^3 cells were seeded in a 6-well plate. After incubation for 2 weeks, the colonies were washed with PBS, fixed with 4% paraformaldehyde, and then stained with crystal violet. The colonies were photographed by the inverted microscope.

2.10. Soft agar colony formation assay

6-well plates were covered with a bottom layer of 2 ml 0.8% agar in 10% FBS-DMEM. Then 3×10^3 cells were suspended in 2 ml of 10% FBS-DMEM containing 0.4% agarose and seeded to the top of a 0.8% agarose. After two weeks, colonies were fixed with 4% paraformaldehyde for 30 min, stained with dilute crystal violet for 20 min. The colonies were photographed by the inverted microscope.

2.11. Determination of ROS production

ROS levels in cells were measured by using 2',7'-dichlorofluorescein diacetate (DCFH-DA). After treatment with erastin (5 μ M), cells were washed with serum-free culture medium and incubated with 4 μ M DCFH-DA in the dark at 37 °C for 30 min. Cells were then washed and harvested, suspended in serum-free culture and fluorescence intensity was measured by flow cytometry.

2.12. Lipid peroxidation

Lipid peroxidation was measured with C11-BODIPY (581/591). When lipid peroxidation increased, the fluorescence is undergoing a shift from red to green fluorescence emission. HT-1080 cells in 6 well plates were incubated with the indicated concentrations of erastin. 2.5 μ M C11-BODIPY(581/591) was added and incubated at 37 °C for 30 min. Excess C11-BODIPY was removed by washing the cells twice with Hanks buffer. Cells were harvested and resuspended for flow cytometry analysis.

2.13. Confocal microscopy assay

The cells were seeded in a chamber confocal dish and treated with the indicated concentration of erastin. Then 581/591 C11- BODIPY (5 μ M) or MitoTracker(100 nM) or RPA(4 μ M) were co-staining with DAPI(10 mg/ml) in the dark for a 30 min incubation. Representative images were viewed under a confocal microscope.

2.14. Measurement of mitochondrial membrane potential (MMP)

The changes of mitochondrial membrane potential (MMP) were observed by tetramethylrhodamine methyl ester (TMRE) probe. HT-1080 cells were treated with 5 μ M erastin for 12 h and then stained with TMRE (100 nM) for 30 min. The stained cells were washed with PBS twice, and analyzed using the flow cytometry.

2.15. Iron assay

The mitochondrial chelatable iron pool was assessed using Rhodamine B-[(1, 10-phenanthroline-5-yl)-aminocarbonyl]benzyl ester (RPA), a Fe²⁺ specific fluorescent sensor. After treatment, cells were harvested and incubated with 2 μ M RPA for 15 min at 37 °C in Hanks balanced salt solution(HBSS), then washed subsequently three times with HBSS. The samples were incubated with dye-free HBSS for another 15 min following washing once with HBSS. Mitochondrial iron was measured using flow cytometry.

2.16. Determination of iron concentrations in isolated mitochondria and cytoplasm by ICP-MS

Total iron concentration was measured using inductively coupled plasma mass spectrometry (ICP-MS, Agilent, Varian) as previously described [20]. In brief, indicated cells were washed, trypsinized and subjected to the subcellular fractions isolation kit (Beyotime, Shanghai, China). Fractions were lysed and quantified by BCA Protein Assay Kit. Each aliquot of the lysed sample was prepared for ICP-MS analyses. Quadruplicate determinations of iron concentration were performed for each sample. The results were conversions from raw ppb values and expressed as pmol/100 mg protein.

2.17. GSH detection

Intracellular GSH levels were examined by using a GSH Assay Kit (Beyotime, Shanghai, China). HT-1080 cells were treated with erastin for 24 h. Then, the subsequent procedures were performed according to the manufacturer's instructions. The experimental data were obtained by a microplate reader.

2.18. Transmission electron microscope (TEM)

After indicated treatment, The cells were fixed by the 2.5% glutaraldehyde solution at 4 °C overnight. After fixation, the samples were dehydrated by a graded series of ethanol, then dehydrated by alcohol and eventually transferred to absolute acetone. Following infiltration with absolute acetone and the final Spurr resin mixture, the samples were embedded, ultrathin sectioned and stained. Finally, the samples were observed in the Hitachi Model H-7650 transmission electron microscope.

2.19. Plasmids

For knockdown of *FXN*, target shRNA sequences were subcloned into pLVX-shRNA Lentivector (Takara). The two shRNA knockdown sequences for *FXN* were forward: 5'- GATCCGCTGGACTCTTTAGCAG AGTTTTCAAGAGAACTCTGCTAAAGAGTCCAGCTTTTTTG-3', and 5'-GATCCGAGACGCCAAACAAGCAAATTTCAAGAGAATTTGCTTGTGG

GCGTCTGCTTTTTTG-3'. Human full-length FXN or FTH cDNA was amplified by RT-PCR using HEK-293 mRNA and verified by sequencing. Then the cDNA was subcloned into pLVX -Neo lentivirus vector (Takara, Dalian, China) by ClonFast Seamless Cloning kit (obio, Nanjing, China). The plasmid of shRNA resistant form of FXN (Res-FXN) was generated according to the described methods by introduced silent changes in the coding region targeted by the shRNA [21].

2.20. Lentiviral transduction

The recombinant lentiviral plasmids were verified by sequencing and co-transfected with pMD2G, pSPAX2 into HEK293 cells to produce recombinant lentiviral. Lentivirus infections were carried out as described previously [12]. Briefly, the cell seeded in 24-well plates reached 70–80% confluence, the 10%-DMEM medium was removed. Cells were then transfected with the corresponding lentivirus. After two days, puromycin or G418 were added for screening. Then the stable cells were maintained in puromycin or G418. The expression efficiency was evaluated by RT-PCR and western blot analysis.

2.21. Western blotting

Following treatment, the cells were lysed in RIPA buffer after washing with PBS and incubated on ice for 30 min. Then cellular debris was removed by centrifugation and the protein concentration was quantified with BCA Protein Assay Kit. Subsequently, equal amounts of protein were separated by SDS-PAGE and transferred to PVDF membranes. The membranes were blocked with 5% skim milk for 1 h and incubated with the primary antibodies at 4 °C overnight. After washing three times with TBST, the membranes were incubated with the secondary antibodies at room temperature for 1 h and washed again. The blots were visualized using a chemiluminescence detection kit ECL-PLUS.

2.22. RNA isolation and quantitative real-time PCR (RT-PCR)

Cells were lysed using Trizol reagent (Invitrogen, USA) and total RNA was extracted with chloroform and isopropyl alcohol. cDNA was then synthesized using a reverse transcription reagent kit (TaKaRa, Dalian, China) according to the manufacturer's protocols. The SYBR Green Master Mix Kit was used for relative quantification of RNA levels according to the manufacturer's instructions. GAPDH was chosen as an internal control. The sequences of the primers were as follows: GAPDH, forward, 5'-GCACCGTCAAGGCTGAGAAC, reverse, 5'-ATGGTGGTGAAGACGCCAGT; FXN, forward, 5'-TAGCAGAGGAAACGCTGGAC, reverse, 5'-ACGCTTAGGTCCACTGGATG. The expression level was normalized to the internal control and determined by a $2^{-\Delta\Delta CT}$ method.

2.23. Determining mitochondrial DNA (mtDNA) copy number

Quantitation of the mitochondrial DNA copy number relative to the nuclear DNA was carried out by using real-time PCR. Primer specific for HGB1 genes were used for the determination of nuclear DNA (nDNA). This primer sequences were used as follows: forward primer, 5'-GTGCACCTGACTCCTGAGGAGA-3'; reverse primer, 5'-CCTTGATACCAACCTGCCAG-3'. And another primer (ND-1) for the detection of mtDNA. The primer sequences were as follows: forward primer, 5'-CCCTA AAA CCCGCCACATCT-3'; reverse primer, 5'-GAGCGATGGTGAGAGCTAA GGT-3'. Q-PCR was performed and the mtDNA copy number was calculated. The thermal cycling conditions for the nDNA and mtDNA amplification were 95 °C for 5 min, followed by 40 cycles of 95 °C for 15 s, 55 °C for 15 s, and 72 °C for 1 min.

2.24. Mouse xenograft model

4–6 weeks old male BALB/c nude mice were used to construct

xenograft models. 2.5×10^6 HT-1080 cells suspended in 0.1 mL PBS were injected subcutaneously into the nude mice. After 7 days, tumor growth was detectable and monitored every 2 days. Tumor volume in mm^3 was determined by measuring the longest diameter (a) and shortest width (b) and calculated by using the following formula: volume (mm^3) = $0.5 \times a \times b^2$. On the 12th day, mice were euthanized and tumors were isolated.

2.25. H&E analysis

Tumors collected from mice were fixed in 4% paraformaldehyde. The paraffin-embedded samples were cut to 4 μm thickness and stained with H&E (Sigma). Stained sections were viewed and photographed under a microscope.

2.26. Immunohistochemistry (IHC)

Tissues were fixed with 4% paraformaldehyde and embedded in paraffin. The paraffin-embedded block tissues were cut into 4 μm sections and followed dewaxed, hydrated and antigen retrieval. After washing with PBS three times, the slides were treated with 3% hydrogen peroxide for 15 min, washed with PBS, blocked with BSA for 15 min at room temperature. Subsequently, anti-FXN antibody (1:200), anti-FTH antibody (1:100) were added to the sections at 4 °C for overnight. The streptavidin peroxidase method was used for signal detection and then stained by diaminobenzidine (DAB) and counterstained with hematoxylin. The sections were observed and photographed under the light microscope. All slides were scored by two independent observers in a blinded fashion.

2.27. Statistical analysis

All statistical calculations were performed using GraphPad Prism (version 7.0). All results were presented as the mean \pm standard deviation (SD). The differences between the two groups were performed by the Student's *t*-test. Comparisons among multiple groups were analyzed by the one-way ANOVA. $P < 0.05$ was considered to be significant.

3. Results

3.1. FXN knockdown repressed the proliferation of HT-1080 cells

FXN stable knockdown cells were generated through lentivirus transduction by two separate short hairpin RNA sequences. Western blot and real-time PCR were used to detect FXN expression. As expected, the knockdown approach dramatically reduced RNA levels and protein expression of FXN in the shRNA cells (Fig. 1A, B). Using these cells, we found that FXN depletion did not lead to cell death, but instead inhibited cellular proliferation (Fig. 1C). To further determine whether the decreased cell proliferation was affected by the cell cycle distribution or not. Cell cycle distribution assay was performed followed by flow cytometry and showed cells were arrested at G0/G1 phase (Fig. 1D, E). Furthermore, the capacity of long-term cell viability between the stably FXN knockdown and control cells was detected by colony formation and soft agar assay (Fig. 1F-I). The results showed FXN suppressed significantly inhibited the capacity of colony formation. Besides, transwell assays were performed to determine the migration of HT-1080 cells and revealed that FXN knockdown dramatically inhibited the migration of HT-1080 cells (Fig. 1J, K). Notably, the high FXN expression indicated a significantly poorer overall survival rate in sarcoma, acute myeloid leukemia, bladder urothelial carcinoma, and adrenocortical carcinoma patients based on The Cancer Genome Atlas (TCGA) datasets (Fig. S1). Taken together, these results discover that FXN plays a vital role in the molecular biological characteristics of cancer and might be a potential indicator of poor prognosis.

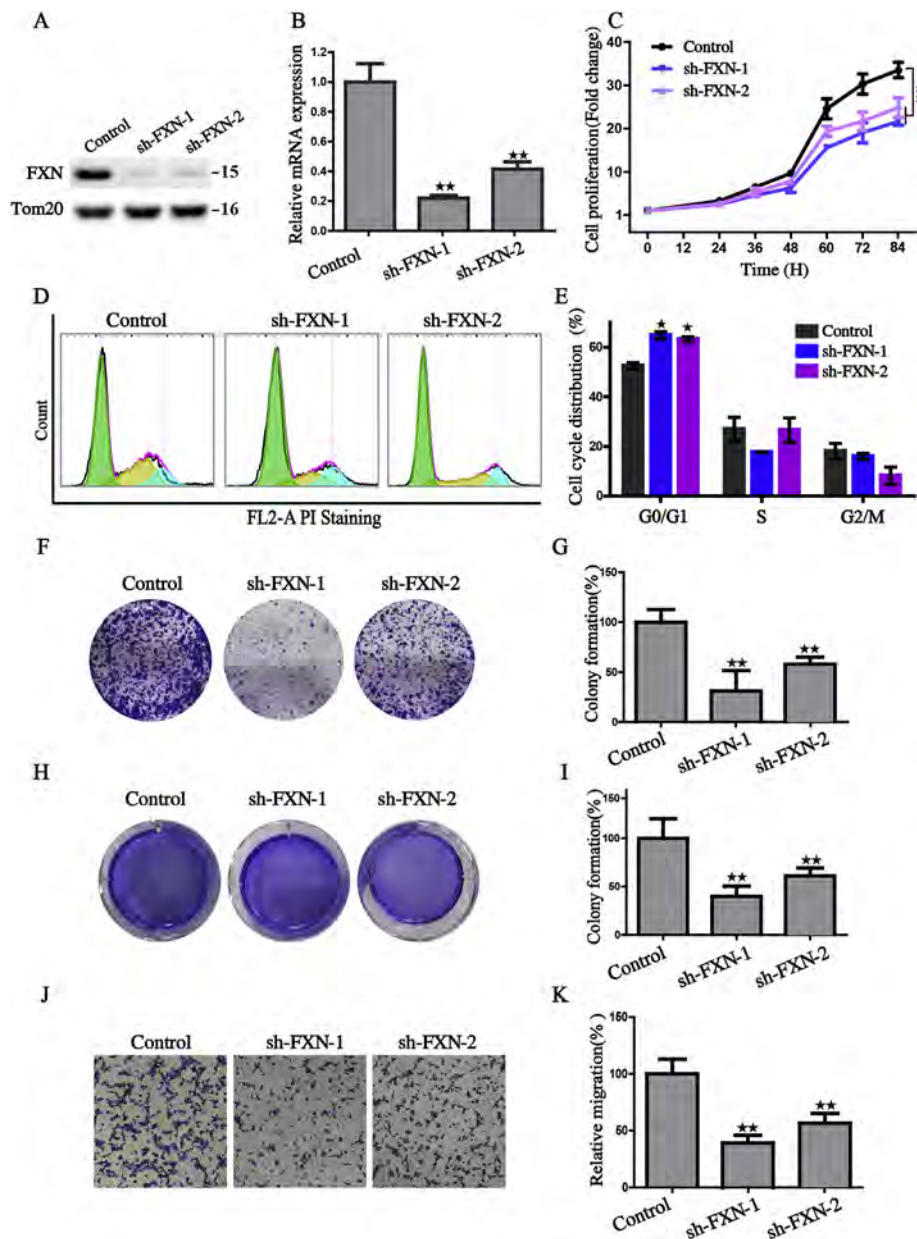


Fig. 1. FXN knockdown repressed the proliferation of HT-1080 cells. (A) Western blot analysis of FXN expression in indicated FXN knockdown and control HT-1080 cells. Tom20 was served as internal loading control. (B) Quantitative real-time PCR analysis of the mRNA of FXN in the three indicated HT-1080 cells. (C) The ability of proliferation was detected by CCK8 assay between control and sh-FXN cells. Induction of cycle arrest in HT-1080 cells was detected by flow cytometry (D-E). Effects of FXN suppression in HT-1080 cells on the proliferation capacity were measured by plate clone formation assay (F-G) and soft agar colony formation assay (H-I), corresponding histograms were shown on the right. Migration of HT-1080 cells was evaluated by transwell assay; corresponding histograms were shown on the right (J-K). All histograms were represented as mean ± SD. **P* < 0.05, ***P* < 0.01 versus control.

3.2. FXN knockdown induced the dysfunction of mitochondria and accumulation of free iron

As FXN is a conserved mitochondrial protein, we next examined the mitochondrial function in the FXN suppressed HT-1080 cells. Firstly, mitochondria were labeled with the mitotracker probe and observed by a confocal laser scanning microscope. The control cells showed a network of elongated mitochondria, in contrast, the FXN knockdown cells appeared fragmentation and accumulation around the nucleus, indicating that FXN depletion resulted in the dysfunction of mitochondrial homeostasis (Fig. 2A). For the close association of mitochondrial morphology with functionality, we next monitored the changes of mitochondrial membrane potential (MMP) through TMRE staining followed by flow cytometry. The results confirmed that the MMP of HT-1080 cells with two different FXN knockdown sequences appeared significant hyperpolarization (Fig. 2B). Earlier published paper has proved that excessive elevating of MMP does not help to accelerate ATP production, but assist the production of free radicals exponentially [22].

The above studies demonstrate that FXN plays a role in maintaining

mitochondrial function; it is unclear the regulation loop between FXN and the activity of oxidative phosphorylation. We next tested the mitochondrial oxygen consumption rate (OCR) by extracellular flux analyzer, which reflected the main mitochondrial function of energy respiration. As showed in Fig. 2C, knockdown of FXN remarkably decreased the oxygen consumption in mitochondria. The basal respiration, maximal respiration and spare respiration, three indices that represent mitochondrial respiration flux revealed a significant decline, demonstrating that FXN knockdown disrupted the process of oxidative phosphorylation (Fig. 2D, E, F). Moreover, ATP production was also calculated and a pronounced loss of ATP exhibited in the FXN knockdown cells, which was unable to meet the cellular ATP demands for supporting cell growth (Fig. 2G). Collectively, the mitochondrial OCR tested by Seahorse XF96 Analyzer uncovered an important link between FXN and oxidative phosphorylation.

Besides energy respiration, ISC assembly is another important process that takes place in mitochondria and considered to be essential for viability. Thus, ISC turnover in iron-sulfur protein was monitored in several ways. Above all, the activity of mitochondrial and cytoplasmic aconitase, important [4Fe- 4S] proteins that catalyze the reaction from

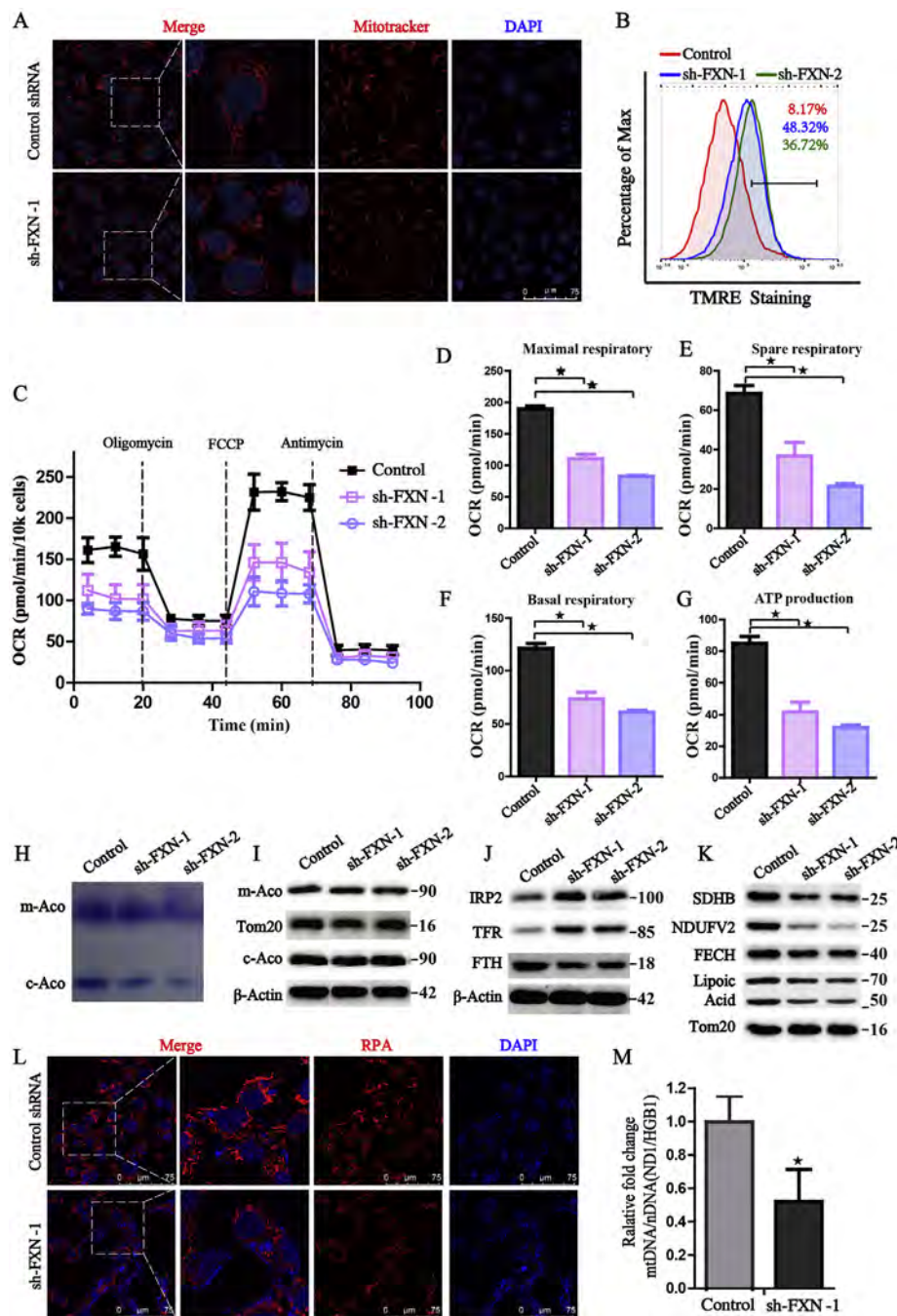


Fig. 2. Suppression of FXN induced the dysfunction of mitochondria and accumulation of free iron. (A) To evaluate mitochondrial morphology, HT-1080 cells were stained with MitoTracker probe (100 nM) and DAPI (10 mg/ml), and then photographed by confocal laser microscope. Scale bars: 75 μ m. (B) Flow cytometry was performed to measure mitochondrial membrane potential (MMP) by TMRE probe (100 nM) in indicated FXN knockdown and control HT-1080 cells. (C) OCR rate was carried out by extracellular flux analyzer after the additions of oligomycin, FCCP and antimycin A. (D-G) The basal respiration, maximal respiration, spare respiration and ATP production were calculated. (H) Mitochondrial and cytoplasmic aconitase activity was analyzed by the in-gel activity assay. (I) The protein levels of mitochondrial and cytoplasmic aconitase were detected by western blot assay. β -actin and Tom20 were used as a loading control. (J-K) Western blot analysis of iron-starvation stress and ISC turnover in iron-sulfur protein. (L) HT-1080 cells were stained with Rhodamine B-[(1,10-phenanthroline-5-yl)-aminocarbonyl]benzyl ester (RPA) probe (4 μ M) and DAPI (10 mg/ml) to detect the cellular labile iron by confocal laser microscope. Scale bars: 75 μ m. (M) The quantitative PCR analysis was performed to measure mitochondrial DNA copy number. Primer specific for HGB1 genes were used for the determination of nuclear DNA (nDNA) and another primer (ND-1) for the detection of mtDNA. * $P < 0.05$, ** $P < 0.01$ versus control.

citric acid to isocitrate, were analyzed by the in-gel activity assay. And the breakdown of mitochondrial ISC assembly resulted in a more dramatic decrease of cytoplasmic aconitase activity than m-aconitase activity, without obvious changes of protein level, demonstrating FXN depletion promoted the loss of the aconitase ISCs (Figs. 2H, I, S2A). It has been reported cellular iron-responsive protein1 (IRP1) and IRP2 play a central role in the regulation of iron metabolism. Apo form of cytoplasmic aconitase transformed into IRP1, which could promote the degradation of ferritin heavy chain (FTH1) mRNA and stabilize transferrin receptor 1 (TFR1) mRNA through IRP-IRE mechanism, thus leading to the iron starvation response. Increased iron starvation response was also confirmed by the upregulated IRP2, TFR and downregulated FTH (Fig. 2J). For the importance of FXN in the de novo ISC biogenesis and impaired mitochondrial OXPHOS in FXN suppressed cells, we also measured the expression of SDHB and NDUFV2, subunits

of complexes I and II whose electron transfer function rely on the intact ISC cluster. Pronounced depletion of SDHB and NDUFV2 was detected in FXN knockdown cells. In addition, the [2Fe-2S] binding FECH, a rate-limiting enzyme in heme biosynthesis, and lipoic acid harbored in PDH E2, KGDH E2 which represented the activity of [4Fe-4S] binding lipoic acid synthase were also significantly decreased (Fig. 2K). These data conclude that FXN depletion reduce steady-state levels of Fe-S cluster dependent proteins as well as reactions and subsequent activation of the iron starvation stress. Besides, in line with previous studies that NRF2, an important transcription factor in regulating cellular redox homeostasis, was downregulated in FXN suppressed cells [23,24]. The mechanism involved may be transcription-independent (protein-protein interaction), for the increased levels of cytosolic Kelch-like ECH-associated protein 1 and a similar level of NRF2 mRNA under FXN suppression (Fig. S 2B, C).

We next used the selective yield fluorescence probe RPA, whose cationic fluorophore could rapidly quench by Fe^{2+} ions, to detect the cellular labile iron. As showed in Fig. 2L, FXN knockdown induced a pronounced accumulation of free Fe^{2+} ions with the decreased fluorescence of RPA. The quantitation of the RPA fluorescence was shown in Fig. S2D. For the observed reduction of OCR, we subsequently monitored the mtDNA copy number, which encodes 13 polypeptides playing crucial roles in the OXPHOS. Consistent with this finding, the mtDNA copy number appeared a clearly decrease in the FXN knockdown cells (Fig. 2M). Collectively, these findings provide a pivotal role of FXN in maintaining the homeostasis of mitochondrial and keep the balance of iron metabolism.

3.3. Suppression of FXN enhanced erastin-induced ferroptosis

We wondered whether suppression of FXN accelerated the process of ferroptosis cell death. Erastin, system X_c^- cystine/glutamate antiporter (xCT) inhibitor, which can depress cysteine levels, was applied to induce ferroptosis in HT-1080 cells. FXN knockdown and control cells were exposed to erastin treatment for 12 h and suppression of FXN expression significantly enhanced erastin-induced cell death. The concentrations of IC50 values for control were evidently higher than that of two FXN knockdown cells, which calculated results were 4.130 μM and 5.527 μM , respectively (Fig. 3A). We obtained a similar phenomenon in U266 and Kasumi-1 cells (Fig. S3 A, B), indicating that FXN sensitized cells to ferroptosis was not restricted to only a single cell lineage. Of note, IKE, another cystine/glutamate antiporter inhibitor, also cooperate with FXN suppression to induce cell death. On the contrary, suppression of FXN expression did not affect cell death induced by other ferroptosis inducers, including RSL3 (GPX4 inhibitor) and BSO (GSH synthase inhibitor) (Fig. S3 C).

Erastin-induced ferroptosis would lead to a disruption of cell membrane permeability, therefore enabled propidium iodide (PI) staining to monitor the progress. The PI staining assay manifested that suppression of FXN expression remarkably induced HT-1080 cell death following erastin treatment. Phase-contrast microscopy also showed FXN depleted cells became shrinking followed by condensation of cytoplasmic constituents, like a “ballooning” phenotype, upon erastin treatment (Fig. 3B). These findings indicated FXN knockdown significantly augmented erastin-induced ferroptotic cell death. In addition, we investigated the proliferation rate of diverse cells exposed to a low concentration of erastin and carboxyfluorescein diacetate succinimidyl ester (CFDA-SE) fluorescence intensity which exponentially decreased with cell proliferation and division was analyzed by flow cytometry. The result indicated that erastin obviously attenuated cell proliferation of HT-1080 cells, which was much more significant upon FXN depletion cells (Fig. 3C). Furthermore, dramatic morphological changes of mitochondria were observed by transmission electron microscopy in FXN depletion cells comprising mitochondrial fragmentation, vacuolization and cristae enlargement, which was aggravated under treatment with erastin (Fig. 3D).

As the accumulation of lipid peroxidation and free iron level were two critical drivers of ferroptosis. The fluorescent staining of BODIPY C11, a sensitive fluorescent reporter for lipid peroxidation, was used to quantify the formation of lipid peroxidation in live cells by flow cytometer and confocal laser microscope. Increasing levels of lipid peroxides were monitored in indicated HT-1080 cells after erastin treated for 12 h, and FXN deletion significantly promoted lipid peroxide formation upon erastin treatment with red fluorescence of the BODIPY shifted to green fluorescence. But FXN depletion alone could not stimulate the accumulation of lipid peroxidation (Fig. 3E, H). Quantitation of the confocal fluorescence was provided in Fig. S3 D. We also discovered similar results that FXN accelerated the accumulation of lipid peroxidation and ROS under the exposure of erastin in U266 cells (Fig. S3 E, F). We next asked whether alteration of GSH level participated in the FXN dependent ferroptosis, and found FXN depletion alone

was not enough to reduce GSH level. But under ferroptotic stress, such as erastin treatment, FXN depletion accelerated the decrease of GSH (Fig. S3 G). Given that iron enables to produce superoxide radicals via the Fenton reaction and result in lipid peroxidation. We next assessed the cellular labile iron pool by RPA probe and found FXN suppression robustly activated the labile iron level under the erastin exposure (Fig. S3 H). In consistent with RPA fluorescence, we also found that FXN depletion activated the iron-starvation response, which was far more robust under the treatment of erastin (Fig. S3 I).

Mitochondrial dysfunction and oxidative stress are the other two characteristics of ferroptosis. We hypothesized that FXN accelerated ferroptosis was associated with the increased of MMP and cytoplasm ROS. Indeed, the elevated levels of MMP and cytoplasm ROS induced by erastin were significantly aggravating by the suppression of FXN (Fig. 3F, G). To further validate that FXN knockdown specifically enhanced the ferroptotic process, we used different signal pathway inhibitors to observe the rescue effect. Notably, erastin-induced cell death was able to reverse by the ferroptosis inhibitor ferrostatin-1 and GSH, but not by the apoptosis inhibitor ZVAD-FMK and necroptosis inhibitor necrosulfonamide (Fig. 3I).

Several studies have revealed that autophagy-dependent degradation of ferritin, a process named ferritinophagy, takes place in ferroptosis. To distinguish whether FXN regulates ferroptosis through modulating autophagy. The conversion of LC3 was detected in FXN depletion and control cells in the absence or presence of erastin. Alterations of FXN expression did not affect the erastin-induced formation of lipidated LC3B (Fig. S3 J). A similar phenomenon was showed that pharmacological inhibition of autophagy by BafA1 could not reverse the FXN induced ferroptosis (Fig. 3I), indicating autophagy was not involved in the FXN dependent ferroptosis. Together, these studies demonstrate that FXN depletion is capable of accelerating erastin induced ferroptosis, most likely due to the breakdown of the ISC biosynthetic machinery and mitochondrial dysfunction.

3.4. Overexpress of FXN contributed to ferroptosis resistance

To shed more light on the specific order of events in modulating mitochondrial function and ferroptosis by FXN, ectopic expression of FXN cell was generated and the proliferation rate was analyzed by the CFDA-SE probe. The results showed that FXN overexpression obviously increased cell proliferation of HT-1080 cells (Fig. 4A). In contrast with mitochondrial dysfunction in FXN suppression cells, ectopic expression of FXN markedly increased mtDNA copy number and decreased the labile iron level (Figs. 4B, D, S4A). Next, we asked whether overexpression of FXN in HT-1080 cells could diminish erastin-induced ferroptosis. As shown in Fig. 4C, cell viability assays of the indicated cells experienced that ectopic expression of FXN sensibly abolished erastin-induced growth inhibition compared to the control and FXN depletion cells. To further verify the specificity of the observed phenomenon, we generated an shRNA-resistant FXN cDNA (Res-FXN) and co-transduced with shFXN. Indeed, overexpression of an shRNA resistant form of FXN efficiently restored the growth inhibition of erastin (Figs. S4B and C). Similarly, expression of Res-FXN conferred resistance to xCT inhibitors, IKE, but not to RSL3 and BSO (Fig. S4D). In consistent with the results of RPA, mitochondrial and cytoplasmic iron measured by ICP-MS demonstrated that knockdown of FXN induced the accumulation of iron in both fractions, while ectopic expression of Res-FXN decreased the level of iron (Figs. S4E and F). Collectively, these findings indicate that expression of FXN is directly responsible for the observed phenotypes and excluding the possibility of off-target effects. More details were found with the mitochondrial morphological changes through MitoTracker fluorescence staining and transmission electron microscopy. The results showed that FXN expression could keep mitochondrial morphology integrity, without severe mitochondrial fragmentation or vacuolization changes under erastin treatment (Fig. 4E, F).

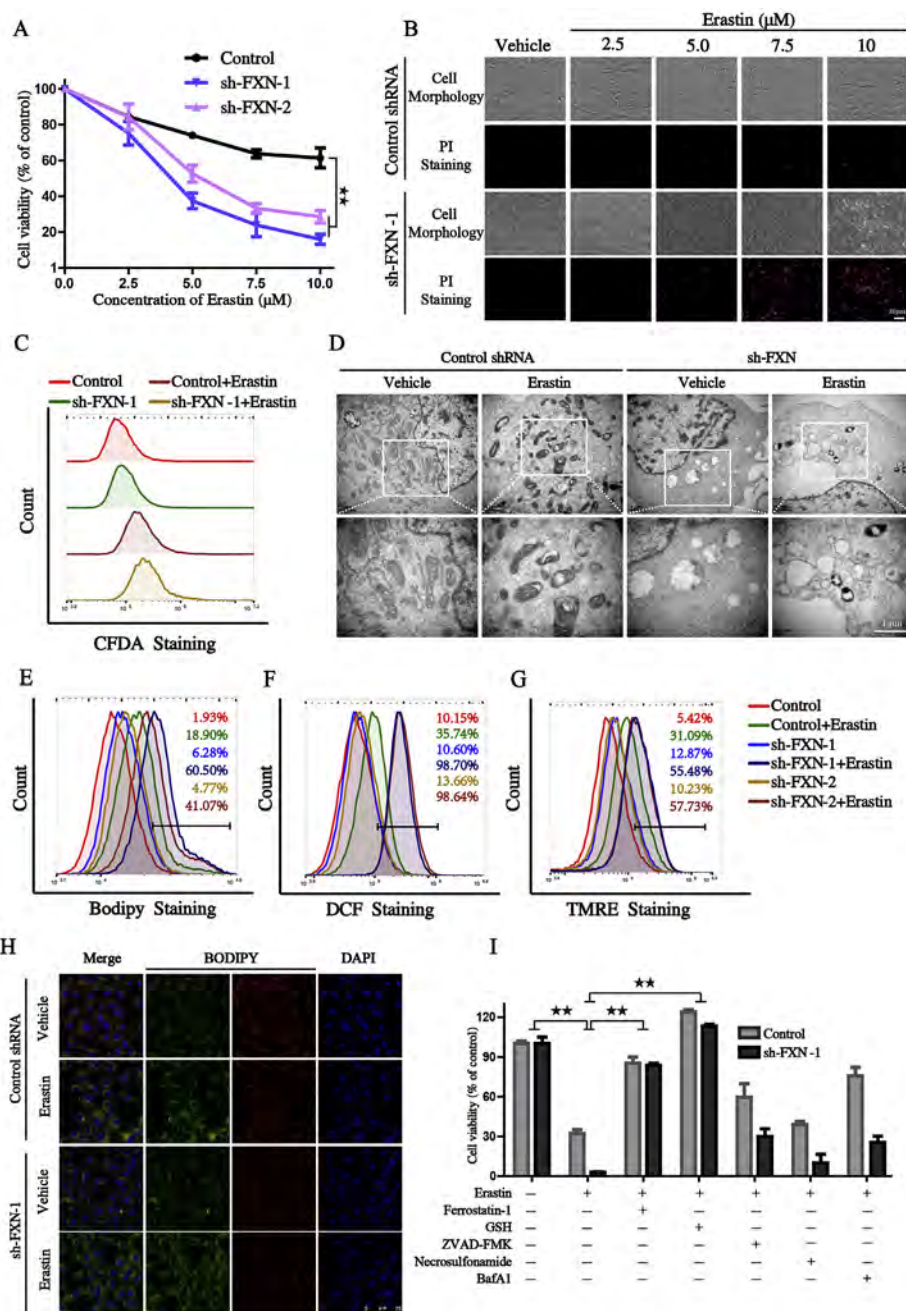


Fig. 3. Suppression of FXN accelerated erastin induced ferroptosis. (A) HT-1080 cells were exposed to various concentrations of erastin for 12 h respectively and followed by CCK8 assay. (B) Propidium iodide positive cells were stained and observed by fluorescent microscopy after erastin exposure for 12 h. Scale bars: 30 μm. (C) CFDA-SE probe (5 μM) stained HT-1080 cells were exposed to 2.5 μM erastin and cultured for 3 days, then subjected to flow cytometry. (D) The morphological changes of mitochondria were detected by transmission electron microscopy (TEM) in the absence or presence of erastin. Flow cytometry was performed to measure lipid peroxides (E), cytoplasm ROS (F), mitochondrial membrane potential(G) after erastin treatment for 12 h in HT-1080 cells. (H) Representative images of BODIPY staining in erastin treated HT-1080 cells which observed by confocal laser microscope. Scale bars: 75 μm. (I) HT-1080 cells were treated with erastin (10 μM) with or without small molecule inhibitor for 12 h and respective cell viability was detected by CCK8. (ferroptosis inhibitor ferrostatin-1, 0.5 μM; GSH, 1 mM; apoptosis inhibitor Z-VAD-FMK, 4 μM; necroptosis inhibitor Necrosulfonamide, 0.5 μM; autophagy inhibitor BafA1, 20 nM). All histograms were represented as mean ± SD. ***P* < 0.01 versus control.

As FXN expression robustly decreased cellular free iron contents, another important question was whether FXN expression could rescue the erastin-induced accumulation of lipid peroxidation. In line with previous findings, FXN expression restored the erastin-challenged lipid peroxidation (Figs. 4G, H, S4G). In addition, ferroptosis inhibitors (ferrostatin-1 and GSH) and DFO restored much less in the FXN over-expression cells than knockdown cells (Fig. 4I). Collectively, these results imply that FXN expression significantly suppresses erastin-induced ferroptosis.

3.5. Free iron depletion enhanced the resistance to ferroptosis in the FXN knockdown cells

The above results suggested that FXN suppression dramatically induced mitochondria dysfunction and activated the iron-starvation response, thus accelerating erastin-challenged ferroptosis. Since ferritin heavy chain (FTH) has ferroxidase activity and oxidizes Fe²⁺ to

catalytically inactive Fe³⁺ and plays a vital role in maintaining iron homeostasis by storing iron in a soluble, non-toxic form. We, therefore, hypothesized that overexpression of FTH might restore dysregulated iron homeostasis in the FXN suppression HT-1080 cells. To test this hypothesis, we reconstituted the expression of iron storage protein FTH in FXN suppression HT-1080 cells and firstly explored the effects on the cell proliferation and mitochondrial function. As expected, the FTH overexpressed cells eliminated the proliferation arrest induced by FXN suppression and accelerated the formation of cell colony, manifesting that iron homeostasis regulation could modulate the injury derive from FXN knockdown (Fig. 5A, B). The quantification of free iron level revealed that FTH expression sensibly blocked the iron accumulation stimulated by FXN suppression (Figs. 5C, D, S5A). Similarity, mitochondria staining also showed a significantly increased network of tubule-shaped morphology, which characteristic for healthy and functional mitochondria under the recombinant expression of FTH in FXN suppression cells (Fig. 5E). Additionally, we evaluated the

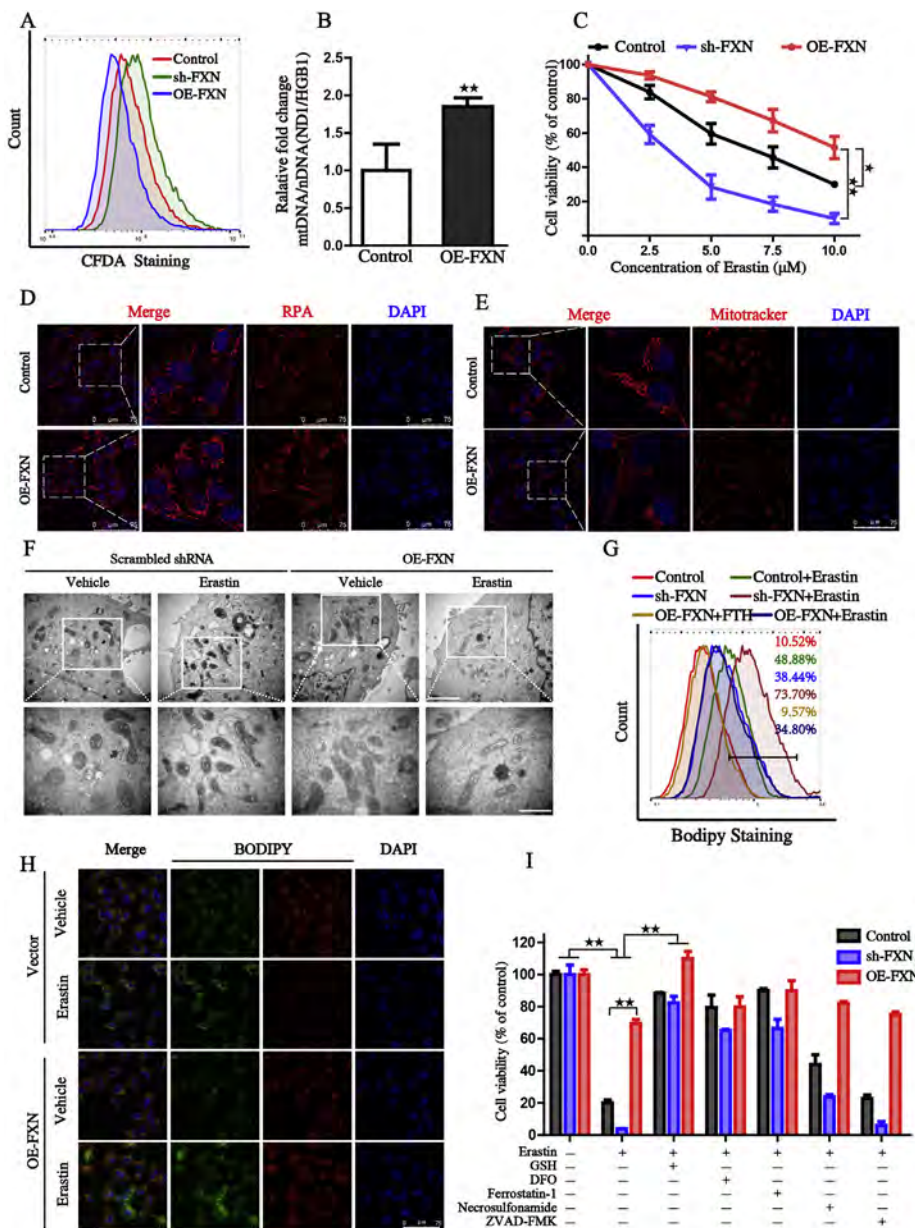


Fig. 4. Enforced expression of FXN contributed to ferroptosis resistance. (A) The proliferation rate was analyzed by the CFDA-SE probe between the indicated cells. (B) Quantitative PCR analysis was performed to measure mtDNA copy number. Primers specific for the HGB1 gene were used for the determination of nuclear DNA (nDNA) and primers specific for ND-1 were used to detect mtDNA. (C) Indicated HT-1080 cells were incubated with different concentrations of erastin for 12 h and cell viability was assayed by CCK8 assay. (D) Intracellular Fe²⁺ was measured by the staining of RPA and photographed by the confocal microscope. Scale bars: 75 μm. (E) MitoTracker Red labeled HT-1080 cells were subjected to the confocal microscope for observing the changes of mitochondrial morphology. Scale bars: 75 μm. (F) The morphological changes of mitochondria were detected by transmission electron microscopy (TEM) in the absence or presence of erastin. Lower scale bars: 0.2 μm. (G-H) To assess lipid ROS production, HT-1080 cells were treated with 5 μM erastin and loaded with BODIPY C11 probe for 30 min followed by flow cytometry measurement (G) and confocal laser microscope (H). Scale bars: 75 μm. (I) Indicated HT-1080 cells were treated with erastin (10 μM) with or without small molecule inhibitor and respective cell viability was detected by CCK8. (ferrostatin-1, 0.5 μM; GSH, 1 mM; iron chelator DFO, 100 μM; Z-VAD-FMK, 4 μM; Necrosulfonamide, 0.5 μM). All histograms were represented as mean ± SD. (For interpretation of the references to colour in this figure legend, the reader is referred to the Web version of this article.) *P < 0.05, **P < 0.01 versus control.

mitochondrial DNA copy and found that FTH recombinant expression could reverse the decrease of mitochondrial DNA copy (Fig. 5F). In summary, these data emphasize the fact that FTH expression restores mitochondrial impairment induced by FXN suppression.

Based on the observed results, we next studied whether FTH expression could rescue the ferroptosis induced by erastin in FXN suppression cells. And the results showed suppression of FXN increased erastin-induced cell death, while reconstituted expression of FTH significantly restored the ferroptosis cell death (Fig. 6A). CCK8 assay was used to evaluate the potency of FTH to restored erastin-induced cell death and results showed FTH fully restored the erastin-induced phenotypes (Fig. 6B). Cells transduced with shFXN displayed noticeable altered mitochondrial shape and size, including mitochondrial fragmentation, vacuolization and loss of cristae enlargement, whereas these phenotypes were reversed by FTH overexpression through reducing cellular iron even with the treatment with erastin (Fig. 6C).

In addition, overexpression of FTH was able to rescue the accumulation of lipid peroxidation and cytoplasm ROS in the FXN knockdown cells upon erastin exposure (Fig. 6D, E). Consistent with these results, pharmacologically chelate free iron by DFO also prevented cell

death of FXN suppression cells to a similar extent as the control under the treatment of erastin (Fig. 4I). In summary, our results emphasize the decisive role of FXN in the regulation of cysteine deprivation-induced ferroptosis through modulating iron homeostasis, which alleviating by the iron depleted.

3.6. Knockdown of FXN inhibited the growth of xenograft in vivo

To evaluate the effect of FXN knockdown on proliferation *in vivo*, FXN suppression HT-1080 cells with or without FTH recombinant expression were subcutaneously injected into nude mice. The growth condition of xenograft tumors was traced, which manifested that FXN silencing indeed blocked the proliferation of tumor *in vivo*, while overexpression of FXN or FTH accelerated the tumor growth (Fig. 7A). Further, H&E and IHC staining were performed and results showed that there were large necrosis areas in FXN silenced tumor tissues, accompanied by nuclear condensation, fragmentation and a significantly decreased Ki-67 expression (Fig. 7B). Inversely FXN overexpression not only maintained the tumor morphology but also promoted the expression of Ki-67. FTH expression was also detected by IHC staining and

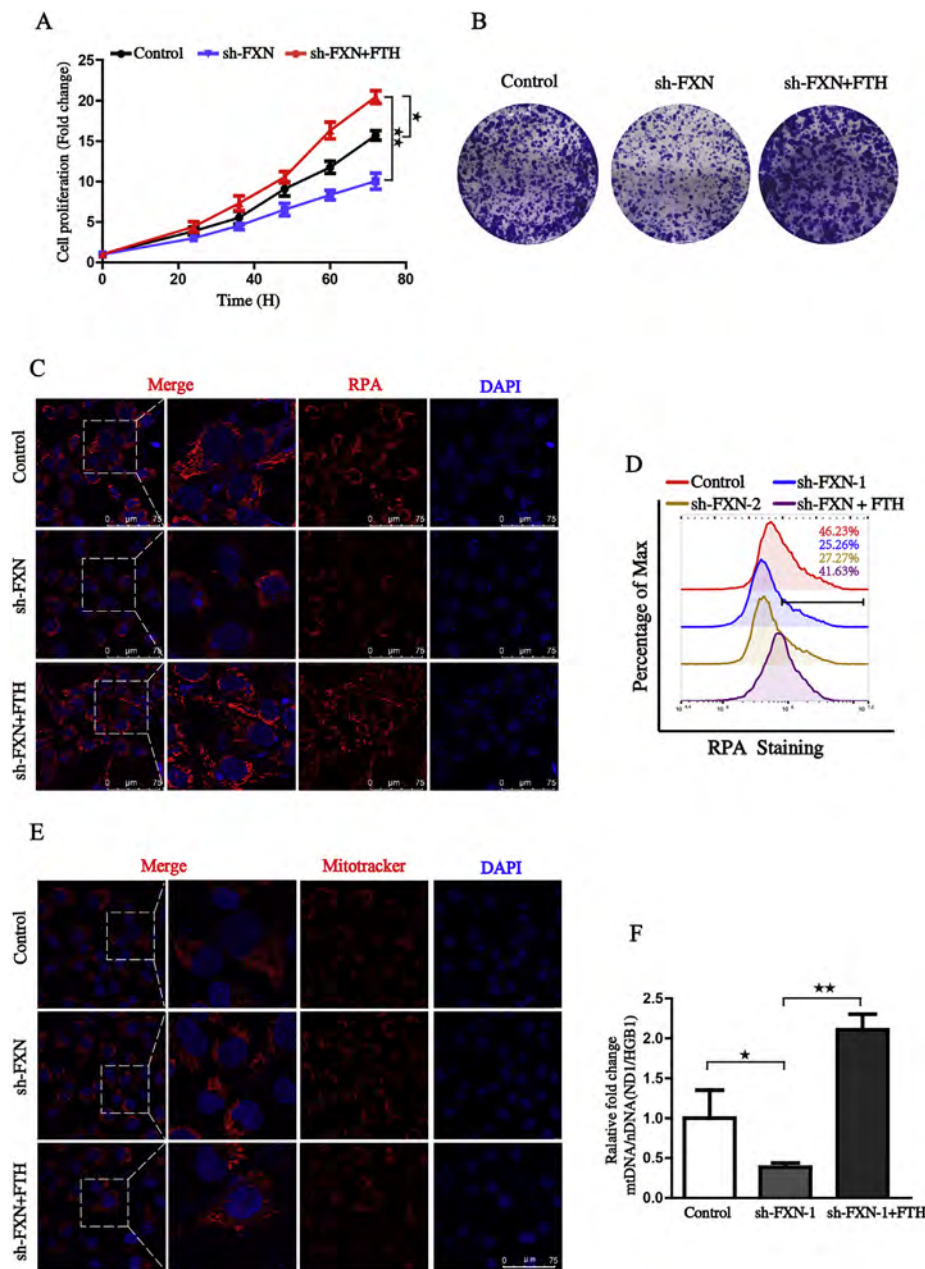


Fig. 5. Overexpress of FTH eliminated the proliferation arrest and mitochondria dysfunction induced by FXN suppression. (A-B) The ability of cell proliferation was measured by CCK8 assay (A) and plate clone formation assay(B) between the three indicated cells. (C-D) To assess intracellular Fe²⁺, cells were stained with RPA probe for 30 min and photographed by a confocal laser microscope(C) or subjected to flow cytometry (D). (E) Cells were stained by MitoTracker Red and mitochondrial morphology changes were observed under the confocal microscope. Scale bars: 75 μ m. (F) The quantitative PCR analysis was performed to measure mtDNA copy number. (For interpretation of the references to colour in this figure legend, the reader is referred to the Web version of this article.) **P* < 0.05, ***P* < 0.01 versus control.

consistent with the data in vitro that FXN knockdown robustly activated iron starving stress and decreased the FTH expression, which significantly restored by FXN overexpression. In addition, FTH expression could also reverse the phenomons exhibited in FXN knockdown xenograft, including inhibited tumors growth and decreased Ki-67 expression. These observations lead to the hypothesis that FXN or the downstream iron homeostasis associated protein can be developed as a therapeutic target, leaving cancer cells at increased risk of ferroptotic cell death.

4. Discussion

Iron is an essential metallic element for all eukaryotes with important functions in the synthesis of iron-sulfur cluster (Fe-S), heme and other cofactors [25–27]. In mammalian cells, Iron homeostasis is tightly regulated by iron regulatory proteins 1 (IRP1) and 2(IRP2) through post-transcriptionally controlling iron metabolism genes via the IRE-IRP mechanism. As shown in several studies, iron excess is

closely related with tumor genesis in some types of human cancers [28]. There is a phenomenon termed iron addiction, which is to say, cancer cells do exhibit an enhanced dependence on iron relatively to healthy cells to enable its growth [3,29]. Supersaturation ferric ion or iron exposure may increase cancer risk. Like two sides of a coin, excess iron loading may also lead to toxicity due to the ability of Fe participating in the production of ROS via Fenton reactions, which may be more pronounced in the highly redox-active mitochondrion. Therefore, the high level of iron may act as a target for cancer therapy [8].

Ferroptosis is a recently identified form of regulated cell death that is distinct from the other types of cell death at morphological, biochemical, and genetic levels and efficiently recovered by ferrostatin-1, GSH and DFO, et, al [4]. Recent study demonstrated that cancer cells depended on high levels of the ISC biosynthetic enzyme NFS1, which was indispensable for Fe-S clusters present in multiple cell essential proteins upon exposure to oxidative damage. Suppression of NFS robustly activates the accumulation of iron and triggers ferroptosis cooperates with cystine/glutamate antiporter inhibitor [30]. Our present

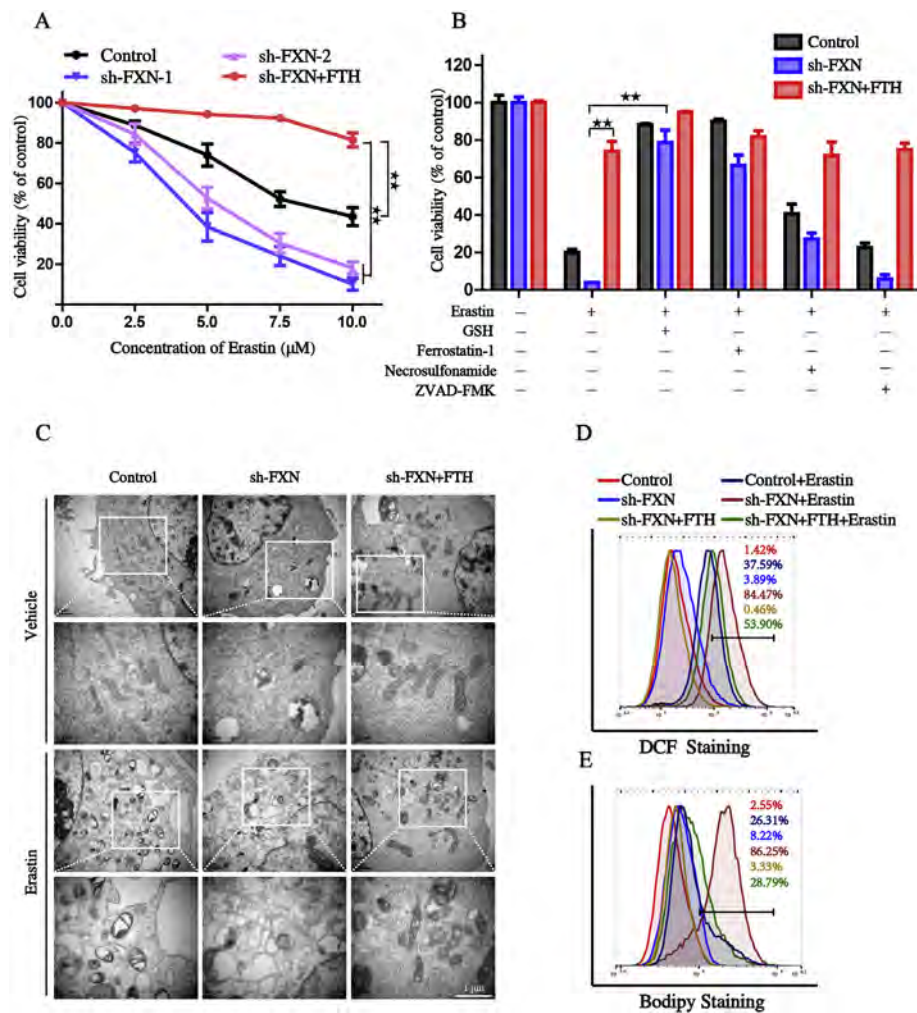


Fig. 6. FTH expression restored the resistance to ferroptosis in FXN knockdown cells. (A) Indicated cells were treated with erastin (0–10 μM) for 12 h and cell viability was assayed by CCK8. (B) HT-1080 cells were treated with erastin (10 μM) for 12 h with or without small molecule inhibitor and respective cell viability was detected by CCK8. (C) The morphological changes of mitochondria were detected by transmission electron microscopy (TEM) in the absence or presence of erastin. Lower scale bars: 0.2 μm. (D) Cells were treated with 5 μM erastin and loaded with DCFH-DA (4 μM) probe for 30 min followed by flow cytometry to assess cytoplasm ROS formation. (E) Indicated HT-1080 cells were treated with erastin (5 μM) for 12 h. Levels of lipid ROS production were detected with BODIPY C11 (2.5 μM) probe by flow cytometry measurement. ****p < 0.01** versus control.

study demonstrated that FXN was a key regulator of ferroptosis by modulating the iron homeostasis and mitochondrial function. Genetic inhibition of FXN significantly repressed the proliferation, destroyed mitochondrial morphology, impeded Fe-S cluster assembly and exacerbated iron accumulation. Erastin further induced dramatic mitochondrial morphological damage in FXN suppressed cells such as enhanced fragmentation and vanished cristae, a phenotype as the hallmarks of ferroptosis, and was consistent with early research. Vice versa, enforced expression of FXN blocked the iron starvation response, MMP hyperpolarization, mitochondrial fragmentation and erastin-induced ferroptosis, confirming that the function of FXN shared beneficial mechanisms for cell survival which acted at upstream of ferroptosis. In particular, both pharmacological and genetic inhibition of iron starvation stress also wholly restored the resistance to ferroptosis in FXN knockdown cells. These results support a mechanistic hypothesis that FXN deficiency accelerate erastin activated ferroptotic cell death.

FXN is a highly conserved protein localizes in the mitochondrial matrix and participates in the biosynthesis of Fe-S cluster. A recent study shows that FXN can activate NFS1 and accelerating a rate-limiting sulfur transfer step of Fe-S cluster assembly by inducing an unusual rearrangement of protein subunits in the de novo assembly complex [15]. In line with the previous finding, suppression of NFS1 make cancer cell sensitive to ferroptosis in vitro and slow tumor growth [30]. The main mechanism of FXN mediated ferroptosis may be the breakdown of the ISC biosynthetic machinery. Mutation of human FXN causes FRDA, a devastating, multi-systemic inherited degenerative syndrome that affects 1 in 50,000 people. Although there is clear evidence demonstrating that FRDA is associated with mitochondrial

dysfunction, mitochondrial iron accumulation, and increased oxidative stress [31], the exact mechanism remains uncertain. Kevin Kemp [32] and Irazusta V et al. [33] demonstrated that cells derived from FRDA patients had deficiencies in defenses against oxidative stress and decreased in superoxide dismutase (SOD) activity. Therefore, Hongting Zhao et al. [34] discovered that mitochondrion-targeted peptide SS-31, a novel mitochondrion-targeted antioxidant, improved the function of mitochondria in FRDA patient-derived cells and might potentially be a new drug for the early treatment of FRDA. Furthermore, Amy Anzovino et al. [23] revealed significant alterations in the cellular redox homeostasis were mediated by Nrf2 deficiency through increased cytosolic Keap1 levels in FRDA mouse model. Similar to earlier studies, Tsilil Ast et al. [35] also verified that FXN depletion resulted in the activation of ATF4-dependent integrated stress response and loss of anti-oxidant NRF2 signaling, which was compromised under hypoxia. NRF2 is an important transcription factor in regulating cellular redox homeostasis through binding antioxidant response elements (AREs). It has been reported NRF2 plays a critical role in mitigating lipid peroxidation [36,37] and its inhibition reverses the resistance to ferroptosis [6,38]. We also identified the downregulation of NRF2 in FXN suppression cells, which might be another factor giving rise to the cells sensitive to ferroptosis. Despite the central role of FXN in oxidative metabolism, it remains unclear whether it plays a central role in cancer progression. In our work, we examined the expression of FXN based on The Cancer Genome Atlas (TCGA) datasets and confirmed that the expression of FXN was much higher in various cancer tissue. And high FXN expression level indicated poor survival of Sarcoma, ACC, BLCA, LAML patients. Overall, the present study exposes FXN as the molecular link

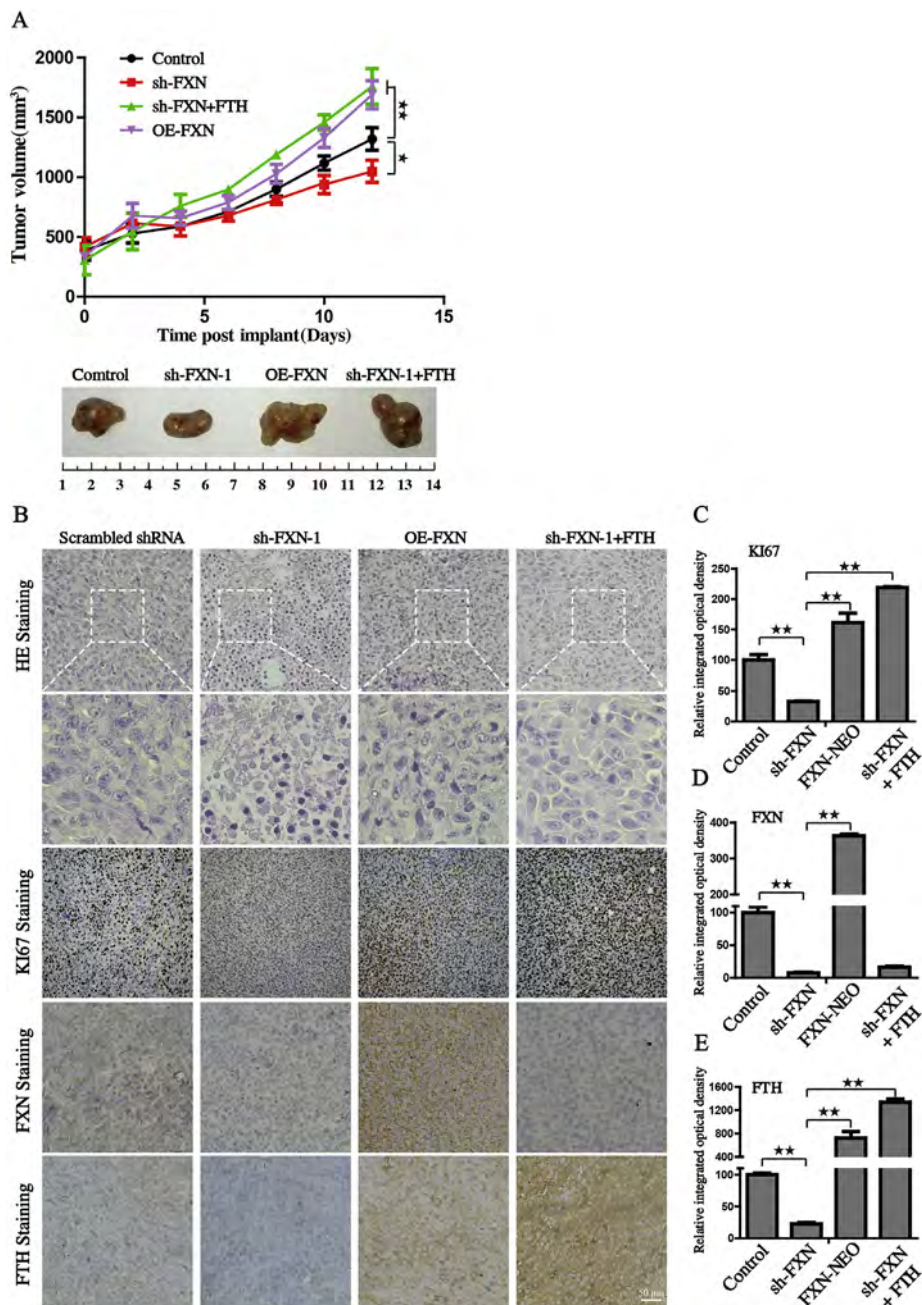


Fig. 7. Knockdown of FXN inhibited the growth of xenograft *in vivo*. (A) The tumor volumes were measured every 2 days and significant inhibition of tumor growth was observed after FXN knockdown. Representative photographs showed the tumor size in mice after the mice were sacrificed. (B) H&E and IHC analysis for Ki67, FXN and FTH in indicated tumor specimens. Scale bars: 50 μ m. (C-E) The Specimens were scored by relative integrated optical density (IOD) value. * $P < 0.05$, ** $P < 0.01$ versus control.

between the oxidative stress signaling and ferroptosis.

It is currently under debate whether mitochondria involved in ferroptosis. Dixon and his co-workers found that mtDNA depleted cancer cell lines did not show a significant difference in ferroptosis sensitivity [39]. Gaschler confirmed that ferrostatin analogs executed the anti-death potency without located in mitochondria [40]. These observations provided evidence arguing against the potential involvement of mitochondria in ferroptosis. By contrast, we evaluated mitochondria from both its morphology and function. Abnormal mitochondrial morphology with decreased or vanished mitochondria cristae was detected in the FXN knockdown cells. The subsequent copy number of mtDNA, encodes 13 polypeptides which play crucial roles in the OXPHOS, was significantly decreased following the knockdown of FXN. As

published before, ISCs undergo spontaneous degradation upon exposure to oxygen and other oxidative stress conditions [41]. Upon FXN suppression, breakdown of the ISC biosynthetic machinery cannot meet the increased demand, ultimately leading to the reduced steady-state levels of Fe-S cluster dependent proteins such as the Fe-S cluster binding subunits of mitochondrial complex and aconitase. All the above data were consistent with the finding FXN deficiency led to dramatically decline of mitochondrial oxygen consumption rate, thus resulting in the insufficient generation of ATP. The detailed investigation of mitochondrial dysfunction provide novel insights into the role of mitochondrial damage in ferroptosis.

It's interesting that FXN suppression stimulates the hyperpolarization of MMP, followed by the eventual collapse leading to cell death,

which is in accordance with previous study [35]. It has been reported that excess hyperpolarization of MMP did not accelerate ATP production, but help to the production of free radicals [22]. In addition, upon pharmacological inhibition of GPX4 or GSH synthase, the downstream components of the ferroptosis signal pathway, ferroptosis can still be triggered independently of FXN depletion. It is likely that iron-starvation stress and mitochondrial dysfunction, associated with FXN deficiency, act at the upstream of ferroptosis, making FXN dispensable for GPX4 inhibition induced ferroptosis. This is in general agreement with earlier reports published by Yang *et al.*, which revealed that mitochondria was involved in the cysteine deprivation-induced ferroptosis but not in glutathione peroxidase-4 (GPX4) inhibition-induced ferroptosis [42]. Collectively, the oxidative stress caused by mitochondrial dysregulation in FXN suppressed cells together with the defective utilization of mitochondrial iron enhancing the erastin-induced ferroptosis, which might potentially be a new drug target.

Declaration of competing interest

The authors declare that there is no conflict of interest.

Acknowledgments

This research was supported by National Science and Technology Major Project for New Drug (No. 2017ZX301033), National Natural Science Foundation of China (81971172), The Key Research and Development Program of Zhejiang Province (WKJ-ZJ-1914), Zhejiang Public Welfare Technology Application Research Project (Grant No. LGF19H080006, LGF20H080005, LY18C090004, 2017C33091), Medical and Health Science and Technology Project of Zhejiang Province (No. 2019RC014, 2019RC115, 2018KY003, 2017KY006, 2017KY209), Zhejiang Students' Science and Technology Innovation Activity Plan (No. 2019R410053).

Appendix A. Supplementary data

Supplementary data to this article can be found online at <https://doi.org/10.1016/j.redox.2020.101483>.

List of abbreviations

FXN	frataxin
shRNA	short hairpin small interfering RNA
PUFAs	polyunsaturated fatty acids
FRDA	Friedreich's ataxia
ISC	Iron-sulfur cluster
ROS	reactive oxygen species
DFO	deferrioxamine
GSH	glutathione
TCGA	The Cancer Genome Atlas
MMP	mitochondrial membrane potential
OCR	oxygen consumption rate
IRP1	iron responsive protein 1
FTH	Ferritin heavy chain
TFR1	transferrin receptor 1
CFDA-SE	carboxyfluorescein diacetate succinimidyl ester
Fer-1	ferrostatin-1
AREs	antioxidant response elements
GPX4	glutathione peroxidase-4
PI	propidium iodide
SOD	superoxide dismutase

References

[1] S. Puig, L. Ramos-Alonso, A.M. Romero, M.T. Martinez-Pastor, The elemental role of iron in DNA synthesis and repair, *Metallomics* 9 (2017) 1483–1500.

- [2] K. Furuyama, K. Kaneko, Iron metabolism in erythroid cells and patients with congenital sideroblastic anemia, *Int. J. Hematol.* 107 (2018) 44–54.
- [3] D.H. Manz, N.L. Blanchette, B.T. Paul, F.M. Torti, S.V. Torti, Iron and cancer: recent insights, *Ann. N. Y. Acad. Sci.* 1368 (2016) 149–161.
- [4] Scott J. Dixon, Kathryn M. Lemberg, Michael R. Lamprecht, R. Skouta, Eleina M. Zaitsev, Caroline E. Gleason, Darpan N. Patel, Andras J. Bauer, Alexandra M. Cantley, Wan S. Yang, et al., Ferroptosis: an iron-dependent form of non-apoptotic cell death, *Cell* 149 (2012) 1060–1072.
- [5] P. A. I. Fl, M. Jm, C. Pj, Regulated necrosis in kidney ischemia-reperfusion injury, *Kidney Int.* 96 (2019) 291–301.
- [6] D. Shin, E.H. Kim, J. Lee, J.L. Roh, Nrf2 inhibition reverses resistance to GPX4 inhibitor-induced ferroptosis in head and neck cancer, *Free Radical Biol. Med.* 129 (2018) 454–462.
- [7] Y. Mou, V. Wang, J. Wu, D. He, C. Zhang, C. Duan, B. Li, Ferroptosis, a new form of cell death: opportunities and challenges in cancer, *J. Hematol. Oncol.* (2019), <https://doi.org/10.1186/s13045-019-0720-y>.
- [8] B. Hassannia, P. Vandenabeele, T. Vanden Berghe, Targeting ferroptosis to iron out cancer, *Canc. Cell* 35 (2019) 830–849.
- [9] T. Hirschhorn, B.R. Stockwell, The development of the concept of ferroptosis, *Free Radical Biol. Med.* (2018), <https://doi.org/10.1016/j.freeradbiomed.2018.09.043>.
- [10] M. Gao, P. Monian, Q. Pan, W. Zhang, J. Xiang, X. Jiang, Ferroptosis is an autophagic cell death process, *Cell Res.* 26 (2016) 1021–1032.
- [11] W. Hou, Y. Xie, X. Song, X. Sun, M.T. Lotze, H.J. Zeh 3rd, R. Kang, D. Tang, Autophagy promotes ferroptosis by degradation of ferritin, *Autophagy* 12 (2016) 1425–1428.
- [12] J. Du, T. Wang, Y. Li, Y. Zhou, X. Wang, X. Yu, X. Ren, Y. An, Y. Wu, W. Sun, DHA inhibits proliferation and induces ferroptosis of leukemia cells through autophagy dependent degradation of ferritin, *Free Radical Biol. Med.* (2018), <https://doi.org/10.1016/j.freeradbiomed.2018.12.011>.
- [13] Y. Yu, Y. Xie, L. Cao, L. Yang, M. Yang, M.T. Lotze, H.J. Zeh, R. Kang, D. Tang, The ferroptosis inducer erastin enhances sensitivity of acute myeloid leukemia cells to chemotherapeutic agents, *Mol. Cell. Oncol.* 2 (2015) e1054549.
- [14] C. Jc, L.B. Ne, Redox-sensing iron-sulfur cluster regulators, *Antioxidants Redox Signal.* 29 (2018) 1809–1829.
- [15] S. Patra, D.P. Barondeau, Mechanism of activation of the human cysteine de-sulfurase complex by frataxin, *Proc. Natl. Acad. Sci. U.S.A.* 116 (2019) 19421–19430.
- [16] S. Pp, V. V. B. K. D.S. P, Iron-sulfur protein assembly in human cells, *Rev. Physiol. Biochem. Pharmacol.* 174 (2018) 25–65.
- [17] C. M, P. H, G. A, K. H, D. A, L. M, F. K, D. P, K. M, Inactivation of the Friedreich ataxia mouse gene leads to early embryonic lethality without iron accumulation, *Hum. Mol. Genet.* 9 (2000) 1219–1226.
- [18] F. Lupoli, T. Vannocci, G. Longo, N. Nicolai, A. Pastore, The role of oxidative stress in Friedreich's ataxia, *FEBS Lett.* 592 (2018) 718–727.
- [19] M.G. Coticelli, S. Xia, D. Lin, T. Lee, L. Terrab, P. Wipf, D. Hury, R. Wilson, Ferroptosis as a novel therapeutic target for Friedreich's ataxia, *J. Pharmacol. Exp. Therapeut.* (2019), <https://doi.org/10.1124/jpet.118.252759>.
- [20] U. Mühlenhoff, J.A. Stadler, N. Richardt, A. Seubert, T. Eickhorst, R.J. Schweyen, R. Lill, G. Wiesenberger, A specific role of the yeast mitochondrial carriers Mrs3/4p in mitochondrial iron acquisition under iron-limiting conditions, *J. Biol. Chem.* 278 (2003) 40612–40620.
- [21] Z. L, B. U, R. JI, An efficient one-step site-directed and site-saturation mutagenesis protocol, *Nucleic Acids Res.* 32 (2004), <https://doi.org/10.1093/nar/gnh110>.
- [22] M. Hüttemann, I. Lee, A. Pecinova, P. Pecina, K. Przyklenk, J.W. Doan, Regulation of oxidative phosphorylation, the mitochondrial membrane potential, and their role in human disease, *J. Bioenerg. Biomembr.* 40 (2008) 445–456.
- [23] A. Anzovino, S. Chiang, B.E. Brown, C.L. Hawkins, D.R. Richardson, M.L. Huang, Molecular alterations in a mouse cardiac model of Friedreich ataxia: an impaired Nrf2 response mediated via upregulation of Keap1 and activation of the Gsk3beta Axis, *Am. J. Pathol.* 187 (2017) 2858–2875.
- [24] Y. Shan, R.A. Schoenfeld, G. Hayashi, E. Napoli, T. Akiyama, M. Iodi Carstens, E.E. Carstens, M.A. Pook, G.A. Cortopassi, Frataxin deficiency leads to defects in expression of antioxidants and Nrf2 expression in Dorsal Root Ganglia of the Friedreich's Ataxia YG8R mouse model, *Antioxidants Redox Signal.* 19 (2013) 1481–1493.
- [25] S. Toyokuni, F. Ito, K. Yamashita, Y. Okazaki, S. Akatsuka, Iron and thiol redox signaling in cancer: an exquisite balance to escape ferroptosis, *Free Radical Biol. Med.* 108 (2017) 610–626.
- [26] H. Harigae, K. Hino, S. Toyokuni, Iron as soul of life on earth revisited: from chemical reaction, ferroptosis to therapeutics, *Free Radical Biol. Med.* 133 (2019) 1–2.
- [27] D.A. Stoyanovsky, Y.Y. Tyurina, I. Shrivastava, I. Bahar, V.A. Tyurin, O. Protchenko, S. Jadhav, S.B. Bolevich, A.V. Kozlov, Y.A. Vladimirov, et al., Iron catalysis of lipid peroxidation in ferroptosis: regulated enzymatic or random free radical reaction? *Free Radical Biol. Med.* 133 (2019) 153–161.
- [28] S.V. Torti, F.M. Torti, Iron and cancer: more ore to be mined, *Nat. Rev. Canc.* 13 (2013) 342, <https://doi.org/10.1038/nrc3495>.
- [29] C. Raggi, E. Gammella, M. Correnti, P. Buratti, E. Forti, J.B. Andersen, G. Alpini, S. Glaser, D. Alvaro, P. Invernizzi, Dysregulation of iron metabolism in cholangiocarcinoma stem-like cells, *Sci. Rep.* 7 (2017) 17667.
- [30] S.W. Alvarez, V.O. Sviderskiy, E.M. Terzi, T. Papagiannakopoulos, A.L. Moreira, S. Adams, D.M. Sabatini, K. Birsoy, R. Possemato, NFS1 undergoes positive selection in lung tumours and protects cells from ferroptosis, *Nature* (2017), <https://doi.org/10.1038/nature24637>.
- [31] R. Abeti, M.H. Parkinson, I.P. Hargreaves, P.R. Angelova, C. Sandi, M.A. Pook, P. Giunti, A.Y. Abramov, Mitochondrial energy imbalance and lipid peroxidation cause cell death in Friedreich's ataxia, *Cell Death Dis.* 7 (2016) e2237, <https://doi.org/10.1038/nature24637>.

- org/10.1038/cddis.2016.111.
- [32] K. Kemp, R. Dey, A. Cook, N. Scolding, A. Wilkins, Mesenchymal stem cell-derived factors restore function to human frataxin-deficient cells, *Cerebellum* 16 (2017) 840–851.
- [33] I. V. O. E, M.-C. A, C. E, R. J, T. J, Yeast frataxin mutants display decreased superoxide dismutase activity crucial to promote protein oxidative damage, *Free Radical Biol. Med.* 48 (2010) 411–420.
- [34] H. Zhao, H. Li, S. Hao, J. Chen, J. Wu, C. Song, M. Zhang, T. Qiao, K. Li, Peptide SS-31 upregulates frataxin expression and improves the quality of mitochondria: implications in the treatment of Friedreich ataxia, *Sci. Rep.* 7 (2017) 9840, <https://doi.org/10.1038/s41598-017-10320-2>.
- [35] T. Ast, J.D. Meisel, S. Patra, H. Wang, R.M.H. Grange, S.H. Kim, S.E. Calvo, L.L. Orefice, F. Nagashima, F. Ichinose, et al., Hypoxia rescues frataxin loss by restoring iron sulfur cluster biogenesis, *Cell* 177 (2019) 1507–1521.
- [36] M. Dodson, R. Castro-Portuguez, D.D. Zhang, NRF2 plays a critical role in mitigating lipid peroxidation and ferroptosis, *Redox Biol.* (2019), <https://doi.org/10.1016/j.redox.2019.101107>.
- [37] X. Sun, Z. Ou, R. Chen, X. Niu, D. Chen, R. Kang, D. Tang, Activation of the p62-Keap1-NRF2 pathway protects against ferroptosis in hepatocellular carcinoma cells, *Hepatology* 63 (2016) 173–184.
- [38] J.L. Roh, E.H. Kim, H. Jang, D. Shin, Nrf2 inhibition reverses the resistance of cisplatin-resistant head and neck cancer cells to artesunate-induced ferroptosis, *Redox Biol.* 11 (2017) 254–262.
- [39] D. Sj, L. Km, L. Mr, S. R, Z. Em, G. Ce, P. Dn, B. Aj, C. Am, Y. Ws, et al., Ferroptosis: an iron-dependent form of nonapoptotic cell death, *Cell* 149 (2012) 1060–1072.
- [40] G. Mm, H. F, F. H, L. A, M. W, S. Br, Determination of the subcellular localization and mechanism of action of ferrostatins in suppressing ferroptosis, *ACS Chem. Biol.* 13 (2018) 1013–1020.
- [41] D.R. Crooks, N. Maio, A.N. Lane, M. Jarnik, R.M. Higashi, R.G. Haller, Y. Yang, T.W. Fan, W.M. Linehan, T.A. Rouault, Acute loss of iron-sulfur clusters results in metabolic reprogramming and generation of lipid droplets in mammalian cells, *J. Biol. Chem.* 293 (2018) 8297–8311.
- [42] M. Gao, J. Yi, J. Zhu, A.M. Minikes, P. Monian, C.B. Thompson, X. Jiang, Role of mitochondria in ferroptosis, *Mol. Cell.* 73 (2019) 354–363.